PHYSICAL REVIEW A **78**, 062510 (2008)

Microwave spectroscopy of high-*L* $n=10$ Rydberg states of argon

M. E. Hanni, Julie A. Keele, and S. R. Lundeen
Department of Physics, Colorado State University, Ft. Collins, Colorado 80523, USA

W. G. Sturrus
Department of Physics, Youngstown State University, Youngstown, Ohio 44555, USA

(Received 6 October 2008; published 31 December 2008)

Twenty-one fine-structure intervals between $n=10$ argon Rydberg levels with $L \geqslant 5$ were measured using microwave spectroscopy, determining the relative positions of all twenty levels with sub-MHz precision. Analysis of the measured pattern using the effective potential model yields determinations of the quadrupole moment, scalar and tensor dipole polarizability, and g factor for the $^2P_{3/2}$ ground state of Ar^+: $Q=-0.520\,83(2)ea_0^2$, $\alpha_{d,0}=6.807(2)a_0^3$, $\alpha_{d,2}=0.077(2)a_0^3$, $g_J=1.335(17)$.

DOI: 10.1103/PhysRevA.78.062510 PACS number(s): 32.30.Bv, 32.10.Dk, 32.10.Fn

I. INTRODUCTION

This paper reports microwave spectroscopy of the nonpenetrating $L \geqslant 5$ $n=10$ Rydberg states of argon. The binding energies of all these states differ only very slightly from the hydrogenic value, defining a fine-structure pattern that is a result of the long-range interactions of the Rydberg electron with the Ar^+ core [1]. Measurements of the pattern can determine the Ar^+ properties, such as electric quadrupole moment and dipole polarizability, that control the strength of these interactions. The relatively high precision of these measurements makes them a valuable check on improving theoretical methods for calculating atomic wave functions and matrix elements. The method used for this study, the resonant excitation Stark ionization spectroscopy (RESIS) technique, has been used previously to study high-*L* fine-structure patterns in a number of different atoms, molecules, and ions [2–5]. The unique aspect of the method is the access it allows to arbitrarily high-*L* levels by high-resolution laser excitation of collisionally populated levels in a Rydberg beam. The fine-structure pattern in argon, such as the pattern studied earlier in neon [2], consists of four different energy levels for each value of Rydberg angular momentum, converging towards the hydrogenic binding energy as *L* increases. The four energies correspond to the four possible orientations of the angular momentum of the $^2P_{3/2}$ ground state of Ar^+ with respect to the angular momentum of the Rydberg electron. A recent study of $n=9$ argon high-*L* Rydberg states, using only optical spectroscopy, gave initial determinations of the quadrupole moment and dipole polarizability of Ar^+, the primary properties controlling the scale of the fine-structure pattern [6]. This study improves on the precision of that study by measuring the fine-structure intervals directly with microwave spectroscopy.

II. EXPERIMENT

The system used to obtain most of the data for this study is shown schematically in Fig. 1. A beam of Ar^+ is formed by a Colutron ion source and accelerated through a 9.5 kV potential. The fast Ar^+ beam then passes through a Rydberg target at (1) in Fig. 1. The target consists of a thermal beam of Rb which is stepwise excited from the ground state to the $9^2F_{7/2}$ state via the $5^2P_{3/2}$ and $4^2D_{5/2}$ states, using three cw diode lasers [7]. Through resonant charge exchange collisions the weakly bound target electrons are transferred to the Ar^+ beam, forming Ar Rydberg levels with similar binding energy. Only a small fraction of the Ar^+ ions ($\sim 1\%$) capture electrons, but the resulting fast Rydberg beam has a large fraction of its population in the $n=10$ level, with a wide range of angular momenta. The fast beam of Ar Rydberg states and the remaining Ar^+ beam then enter the preionizer at (2) in Fig. 1. This electrode is held at a potential of 10 kV, creating a 20 kV/cm electric field in this region. The potential repels any remaining Ar^+ beam back towards the source and the large field ionizes any Ar atoms that may have captured an electron into a state with $n \geqslant 15$. The remaining Ar beam then passes through the CO_2 laser interaction region (LIR) where a fixed frequency CO_2 laser beam intersects the Rydberg beam at a variable angle, denoted θ in Fig. 1. As θ is varied the frequency of the laser, as seen in the rest frame of the Ar beam, is Doppler-tuned according to Eq. (1),

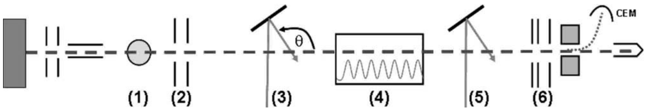

FIG. 1. Schematic of the RESIS apparatus used for this study. The fast Ar beam is created by passing a 9.5 keV Ar^+ ion beam through a Rydberg target at 1 in the figure. Highly excited Rydberg states with $n \geqslant 15$, are ionized at 2. Any residual Ar^+ beam is deflected out of the beam's path at 2 as well. At 5 a fixed frequency CO_2 is used to selectively excite high angular momentum states from $n=10$ to $n=30$ or 31. These states are then ionized and energy tagged at 6, and detected by the channel electron multiplier (CEM). For the microwave study presented in this paper the first CO_2 laser interaction region (LIR) at 3 was used to initially deplete the population of a specific $10L_K$ level. The beam then passed into the microwave interaction region at 4 where a microwave electric field is applied at a frequency near an electric dipole allowed transition from the $10L_K$ level to another $n=10$ fine-structure level. If the microwaves cause a resonant transition, this results in additional excitation at 5 and ionization at 6.

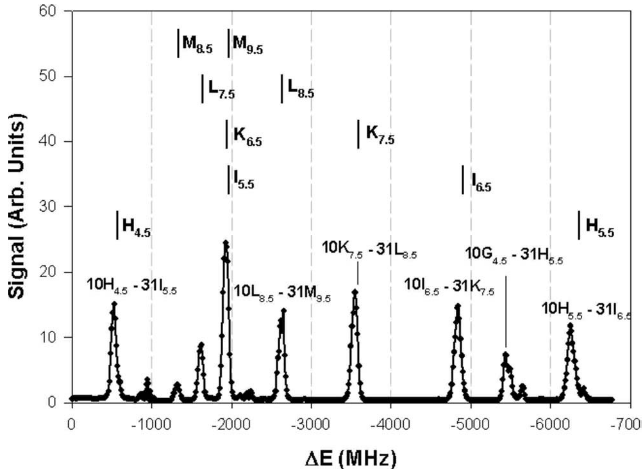

FIG. 2. RESIS optical signal as a function of the energy difference between the Doppler tuned laser frequency and the $n=10$ to $n'=31$ hydrogenic energy. The peaks are identified using the fine-structure pattern for $n=10$ Ar calculated using previous measurements [6] and included as a superimposed level diagram in the figure.

$$v_L' = \frac{v_L}{\sqrt{1-\beta^2}}(1+\beta\cos\theta). \tag{1}$$

The laser selectively excites particular $n=10$ fine-structure levels to a much higher level ($n'=30$ or 31) previously emptied in the preionizer. These highly excited Rydberg atoms are then Stark ionized at (6) in Fig. 1, energy tagged to distinguish them from ions formed by collisions with background gas, and deflected into a channel electron multiplier (CEM) monitoring the Stark ionization current. Typical system pressures in the LIR region were 10^{-6} Torr. Pressures in the detector region were at least an order of magnitude lower.

Because of the low velocity of the Rydberg beam ($v/c=0.000\,711\,3$), two CO_2 lines, the $10R(32)$ at 983.252 cm^{-1} and the $10R(20)$ at 975.930 cm^{-1} were used to access all the $n=10$ Rydberg levels studied here. Figure 2 shows a portion of a $n=10$ to $n=31$ optical spectrum obtained with the $10R(32)$ CO_2 laser line by varying θ. The x axis shows the difference between the Doppler-tuned laser frequency and the nonrelativistic hydrogenic 10–31 transition frequency, 983.169 cm^{-1}. Also shown in Fig. 2, on the same scale as the excitation spectrum, is a partial level diagram for the $n=10$ Rydberg levels being excited. These are labeled in the notation L_K, where L denotes the angular momentum of the $n=10$ level, in spectroscopic notation, and K is the total angular momentum exclusive of Rydberg spin,

$$\vec{K} = \vec{L} + \vec{J}_C.$$

Not resolved in Fig. 2 is the doublet splitting of each level due to the Rydberg electron's spin.

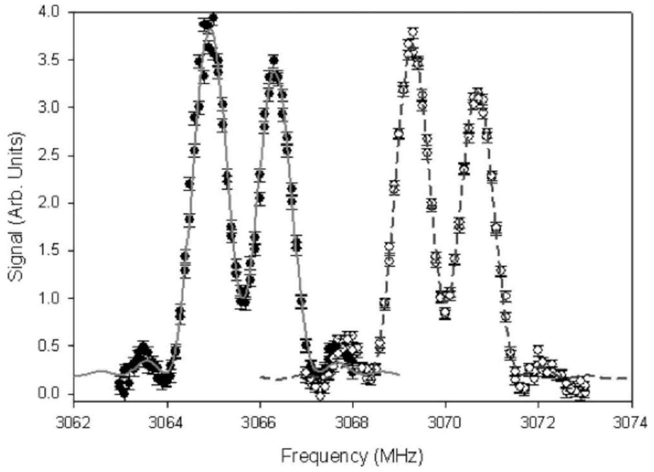

FIG. 3. Spin resolved microwave signal for the transition between the $10I_{7.5}$-$10K_{8.5}$ states, showing the Doppler shift due to the different directions of propagation of the microwave field with respect to the beam direction of propagation as well as the two signal peaks resulting from resolution of the Rydberg electron's spin components. The solid line through the points represents the sinc-squared fit used to determine the center of the transition frequency.

Precise determination of the fine-structure intervals is obtained by driving microwave transitions directly between different $n=10$ levels, using the selective RESIS ionization of specific fine-structure levels to detect the microwave transitions. With this method, the Rydberg beam first passes through a LIR, at (3) in Fig. 1, which saturates an excitation transition from $10L_K$ to $31(L+1)_{K+1}$, reducing the population of the $10L_K$ level by about a factor of 2. The beam then passes into the microwave interaction region, at (4) in Fig. 1, where a microwave electric field is applied at a frequency near an electric dipole allowed transition from the $10L_K$ level to another $n=10$ fine-structure level. When the applied frequency matches the resonant frequency for the transition, the populations of the two levels will equalize, provided that enough power is supplied to saturate the transition. The resulting change in the population of the $10L_K$ level, if any, is detected by a second LIR, at (5) in Fig. 1, which is tuned to the same transition as the first LIR. In the absence of a microwave-induced population change the second LIR will have little effect, since it is tuned to a transition that was saturated in the first LIR. However, any increase in the $10L_K$ population will allow additional excitation to the high-n level and a resulting increase in the Stark ionization current. Any such increase is taken to be the microwave signal. Two typical microwave resonance signals are shown in Figs. 3 and 4. The frequency resolution is determined by the transit time through the microwave region, and is approximately 1.0 MHz. In some cases, e.g., Fig. 3, this resolves the two transitions corresponding to the two possible orientations of the Rydberg electron spin. In other cases, e.g., Fig. 4, these two transitions are unresolved.

By tuning each of the LIRs to the resolved lines in the optical spectrum and scanning through the microwave frequency twenty-one different transitions among the $n=10$ Ar Rydberg levels were measured. These transitions, illustrated in Fig. 5, determine the relative positions of all $n=10$ fine-structure levels with $L \geqslant 5$. Notice that the $I_{5.5}$ and $K_{6.5}$ levels are nearly degenerate, separated by only about 20 MHz. This makes them very sensitive to perturbation by stray electric fields. The intervals shown as double lines in Fig. 5 were also measured in an earlier study [8]. Those measurements,

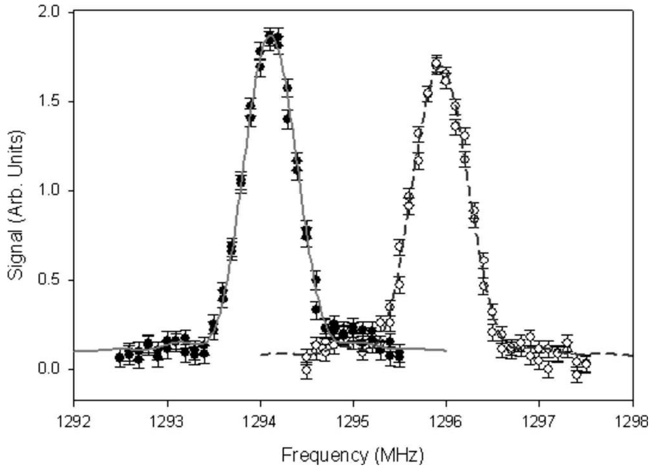

FIG. 4. Spin unresolved microwave signal for the transition between the $10L_{6.5}$-$10M_{7.5}$ states, showing the Doppler shift due to the different directions of propagation of the microwave field with respect to the beam direction of propagation. The solid line through the points represents the sinc-squared fit used to determine the center of the transition frequency.

reported here, were obtained with a similar method, but using a different apparatus, the same apparatus used for a study of H_2 and D_2 Rydberg levels and fully described in that report [4]. The dashed-dotted line in Fig. 5 indicates a two-photon transition that assisted in the location of the $H_{3.5}$ level.

The microwave electric fields were applied in 50 Ω TEM transmission lines in which the direction of microwave propagation could be chosen either parallel or antiparallel to the Rydberg beam velocity. The measurements used two eccentric cylindrical transmission lines [9] similar to region A in Ref. [4]. One region had diameters of the outer and inner conductors of 1.61 and 0.32 cm, respectively. The other had diameters of 3.41 and 0.95 cm. The microwave interaction regions (regions C and D in Ref. [4]) used in the earlier study had larger cross sectional areas, resulting in lower values of the stray electric fields inside the regions. Due to the importance of Stark shift corrections in the present study, the earlier measurement of the Stark sensitive $K_{6.5}$-$L_{7.5}$ transition is an especially valuable addition to the total data set.

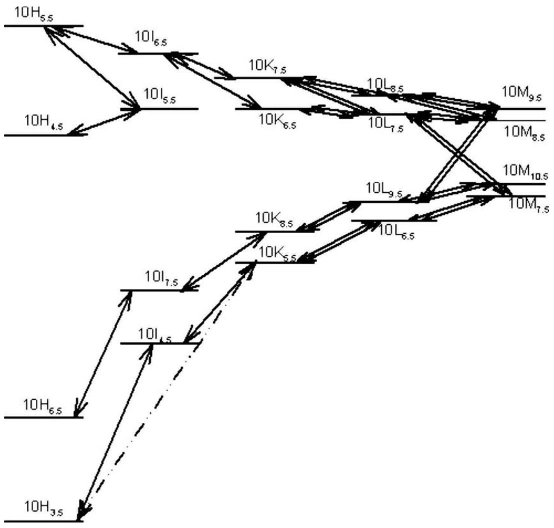

FIG. 5. Level diagram for the $n=10$ argon Rydberg levels, illustrating the 21 observed fine-structure intervals measured in this study. The double arrows represent transitions that were also measured in an independent study performed earlier. The dashed—dotted line indicates a two-photon transition used to assist in the location of the $H_{3.5}$ level.

III. DATA ANALYSIS

A. Spin structure

When signals are observed with a doublet structure, as illustrated for one case in Fig. 3, this represents resolution of transitions corresponding to the two possible values of

$$\vec{J} = \vec{K} + \vec{S}_R,$$

where S_R is the spin of the Rydberg electron. A strong selection rule dictates $\Delta J = \Delta K$ transitions are much stronger than the $\Delta J = 0$ transitions, so at most two components are observed. For the balance of this report, the fine-structure intervals we report represent intervals between the centers of gravity of the $J = K \pm 1/2$ levels for each L_K level.

The spin structure is expected to be due to the magnetic interactions of the Rydberg electron spin with magnetic fields due to its orbital motion around the core ion and with magnetic fields produced by the magnetic moment of the Ar^+ ion core, as described by the spin Hamiltonian of Eq. (2),

$$H_{Spin} = \alpha^2\left[\frac{1}{2}\frac{\vec{L}\cdot\vec{S}_R}{r^3} + \frac{g_J}{2}\frac{\vec{J}_C\cdot(1-3\hat{r}\hat{r})\cdot\vec{S}_R}{r^3}\right], \tag{2}$$

where g_J, the g factor of the ${}^2P_{3/2}$ Ar^+ ground state is expected to be approximately $4/3$. Equation (2) predicts that the order of the spin levels is normal, i.e., the state with higher J is higher in energy. Spin splittings for all of the transitions were predicted from Eq. (2), with the results shown in Table I, column 3. In cases where the two spin components were resolved experimentally, such as Fig. 3, a value of the spin splitting was obtained by separately fitting each transition frequency. The results are shown in column 2 of Table I. Comparison with column 3 indicates, with one exception, agreement between the measured and predicted splittings to within a few percent. Cases where no spin splitting was resolved corresponded consistently to either (1) a predicted splitting less than 0.6 MHz, making it unresolvable, or (2) a transition involving one of the highly Stark sensitive $I_{5.5}$ or $K_{6.5}$ levels, where Stark broadening prevented resolution. We take this as confirmation that the model of Eq. (2) is sufficiently accurate to extract the centers of gravity of the fine-structure intervals. The exception to this agreement is the splitting of the $H_{3.5}$ level, which is due to perturbation by the $F_{3.5}$ state, as discussed in Appendix A.

The intervals between centers of gravity were extracted from the measured spectra by fitting the data to a superposition of lines separated by the frequency offsets, δ_1 and δ_2, calculated from Eq. (2),

TABLE I. Observed and predicted spin splitting intervals for microwave transitions in $n=10$ argon. The transitions are identified in column 1, and when a splitting was resolved experimentally the fitted value is shown in column 2. Column 3 shows, for comparison, the splitting calculated from Eq. (2). The value in column 4 is the ratio of the observed value to the predicted value. The first comparison shown, the $H_{3.5}$-$I_{4.5}$ transition, is the only obvious discrepancy.

Transition	Observed splitting (MHz)	Predicted splitting (MHz)	Ratio
$H_{3.5}$-$I_{4.5}$	15.955(23)	0.547	29.16(4)
$H_{4.5}$-$I_{5.5}$	⋯	0.768	⋯
$H_{5.5}$-$I_{6.5}$	1.296(11)	1.352	0.959(8)
$H_{5.5}$-$I_{5.5}$	⋯	2.213	⋯
$I_{4.5}$-$K_{5.5}$	⋯	0.467	⋯
$I_{5.5}$-$K_{6.5}$	⋯	0.616	⋯
$I_{6.5}$-$K_{7.5}$	0.937(11)	0.918	1.021(11)
$I_{7.5}$-$K_{8.5}$	1.42(2)	1.383	1.03(5)
$K_{5.5}$-$L_{6.5}$	⋯	0.368	⋯
$K_{6.5}$-$L_{7.5}$	⋯	0.468	⋯
$K_{7.5}$-$L_{7.5}$	1.002(19)	1.027	0.976(19)
$K_{7.5}$-$L_{8.5}$	0.69(3)	0.643	1.07(5)
$K_{8.5}$-$L_{9.5}$	0.920(15)	0.901	1.021(17)
$L_{6.5}$-$M_{7.5}$		0.290	
$L_{7.5}$-$M_{8.5}$	⋯	0.355	⋯
$L_{7.5}$-$M_{7.5}$	⋯	0.552	⋯
$L_{8.5}$-$M_{9.5}$	0.54(5)	0.465	1.16(11)
$L_{8.5}$-$M_{8.5}$	0.74(4)	0.739	1.00(5)
$L_{9.5}$-$M_{10.5}$	0.64(4)	0.618	1.04(6)
$L_{9.5}$-$M_{9.5}$	1.03(14)	0.973	1.06(14)

$$S(f) = y_0 + a_1\left(\frac{\sin\{[f-(f_0+\delta_1)]\pi T\}}{[f-(f_0+\delta_1)]\pi T}\right)^2 + a_2\left(\frac{\sin\{[f-(f_0+\delta_2)]\pi T\}}{[f-(f_0+\delta_2)]\pi T}\right)^2. \tag{3}$$

Figure 6 illustrates, with the example of the $I_{7.5}$ to $K_{8.5}$ transition, the connection between f_0, the interval between centers of gravity, ΔE_1 and ΔE_2, the doublet splittings of the two levels, and δ_1 and δ_2. In cases where the two spin components were well resolved, as in Fig. 3, the relative amplitudes a_1 and a_2 were freely varied, along with the frequency f_0, interaction time T, and offset y_0. Two such fits are shown in Fig. 3, one for each direction of propagation of the microwave field. The fitted values of a_1 and a_2 were found to be consistent, to within a precision of 15%, with the ratio of statistical weights of the two line components, as given by Eq. (4),

$$\frac{a_2}{a_1} \cong \frac{2J_2+1}{2J_1+1}, \tag{4}$$

where J_i is the total angular momentum of the lower L component of the line. In cases where the spin splitting was unresolved, the ratio of amplitudes was fixed with Eq. (4), and an additional uncertainty equal to 5% of the calculated spin splitting, $\delta_1-\delta_2$, was added to the statistical uncertainty of f_0. Each transition was measured at least three times, for both directions of microwave propagation. The geometric mean of the fitted f_0 for the two directions of propagation was taken to represent the frequency interval in the atom's rest frame. These raw results are shown in Table II, where column 1 identifies the transition, column 2 indicates the number of independent measurements, and column 3 shows the straight average of the N independent measurements, prior to any Stark shift correction. The uncertainty shown there is the larger of the internal or external errors of the mean. Two transitions, labeled D and F in Table II received special treatment relating to treatment of Stark shifts.

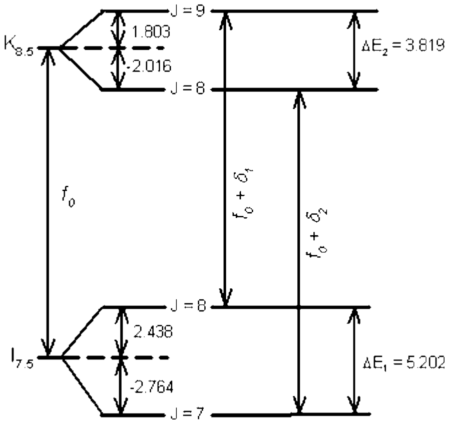

FIG. 6. Example level diagram illustrating the spin splitting of two Rydberg levels, the $I_{7.5}$ and $K_{8.5}$, and the resulting separation of the two allowed transitions between these levels. The difference in energy between the centers of gravity for the two levels is shown as f_0. The net splitting of each level, ΔE_i is shown, as is the separation of each spin level from the corresponding center of gravity. The frequency offsets are $\delta_1=-0.635$ and $\delta_2=0.748$ for this transition.

Another exception to this method is the $H_{3.5}$ to $I_{4.5}$ interval. The anomalously large spin splitting shown in Table I is clearly not consistent with the model of Eq. (2), making it necessary to use some other method to determine the position of the center of gravity of the $H_{3.5}$ level. Since both the $I_{4.5}$ and the $K_{5.5}$ levels show no indication of deviation from the spin-splitting model, it was assumed that they were accurately given by Eq. (2). By combining observations of the two spin components of the $H_{3.5}$-$I_{4.5}$ transition with observations of the two spin components of the two-photon $H_{3.5}$-$K_{5.5}$ transition the following was determined:

(1) The order of spin components in the $H_{3.5}$ level is normal and their energy difference is 18.55(2) MHz. Note that this is much larger than the 3.15 MHz predicted by Eq. (2).

(2) The center of gravity of the two spin components of the $H_{3.5}$ level lies 9384.725(12) MHz below the center of gravity of the $I_{4.5}$ level. Like the spin splitting, this position is also found to be anomalous when analyzed using the effective potential model. Both anomalies are explained by perturbation by the $10F_{3.5}$ level, as discussed in Appendix A.

B. Electric field corrections

By far the most important systematic correction necessary in this study involves the Stark shifts that result from the

TABLE II. Summary of the measured values of f_0 for the 21 transitions of this study. These represent the straight average of several repeated measurements, each of which included measurements with both directions of propagation of the microwave field. Column 1 identifies the transition. Column 2 shows the number of independent measurements. Column 3 gives the average result, before any systematic corrections, with an uncertainty given by the larger of the internal or external errors. Column 4 shows the average Stark shift correction applied, as discussed in the text, and column 7 gives the corrected result. Column 5 shows the additional uncertainty assigned in cases where the two spin components were unresolved. Column 6 shows the statistical uncertainty in the corrected result, the larger of the internal and external errors. The uncertainty shown in column 7 is the quadrature sum of the uncertainties shown in columns 4, 5, and 6.

Transition	N	f_0 (MHz)	Δf_E (σ_E)	σ_{Spin}	σ_{Stat}	ΔE (MHz)
$L_{6.5}$-$M_{7.5}$	4	1295.023(6)	−0.007(3)	0.015	0.004	1295.016(16)
$L_{7.5}$-$M_{7.5}$	4	4313.598(27)	+0.047(22)	0.028	0.027	4313.645(45)
$L_{7.5}$-$M_{8.5}$	4	309.750(10)	−0.005(2)	0.018	0.008	309.745(20)
$L_{8.5}$-$M_{8.5}$	4	1302.869(16)	+0.028(10)	0.037	0.026	1302.897(46)
$L_{8.5}$-$M_{9.5}$	4	668.212(17)	−0.012(4)	0.023	0.014	668.201(27)
$L_{9.5}$-$M_{9.5}$	4	4928.966(36)	+0.020(10)	0.049	0.036	4928.986(62)
$L_{9.5}$-$M_{10.5}$	4	921.453(7)	−0.010(4)	0.031	0.003	921.443(31)
$K_{5.5}$-$L_{6.5}$	4	2198.870(6)	−0.003(1)	0.018	0.004	2198.867(19)
$K_{6.5}$-$L_{7.5}(F)$	4	N/A	N/A	N/A	N/A	302.12(14)
$K_{7.5}$-$L_{7.5}$	4	1946.858(12)	−0.026(10)	0.000	0.004	1946.832(11)
$K_{7.5}$-$L_{8.5}$	4	953.733(7)	−0.005(2)	0.032	0.006	953.728(33)
$K_{8.5}$-$L_{9.5}$	4	1601.658(3)	−0.004(1)	0.000	0.003	1601.654(3)
$I_{4.5}$-$K_{5.5}$	3	4310.192(4)	−0.001(0)	0.023	0.004	4310.191(23)
$I_{6.5}$-$K_{6.5}$	3	2956.60(18)	−1.57(50)	0.074	0.23	2955.04(56)
$I_{6.5}$-$K_{7.5}$	3	1310.115(2)	+0.002(1)	0.000	0.002	1310.117(2)
$I_{7.5}$-$K_{8.5}$	3	3067.754(5)	−0.001(0)	0.000	0.006	3067.754(6)
$H_{5.5}$-$I_{5.5}$	3	4386.63(84)	+2.79(90)	0.111	0.37	4389.42(98)
$H_{5.5}$-$I_{6.5}$	3	1454.285(43)	−0.121(41)	0.000	0.009	1454.165(42)
$H_{6.5}$-$I_{7.5}$	3	6726.675(9)	+0.003(1)	0.000	0.009	6726.678(9)
$H_{4.5}$-$I_{5.5}(D)$	3	N/A	N/A	N/A	N/A	1398.13(20)
$H_{3.5}$-$I_{4.5}$	4	9384.726(12)	−0.001(0)	N/A	0.012	9384.725(12)

presence of stray electric fields within the microwave interaction region. Motional electric fields due to the Earth's magnetic field were reduced to <0.01 V/cm by a double magnetic shield. Stray fields up to an order of magnitude larger than this were found to occur within the interaction region, probably due to charging of nominally conducting surfaces and were especially significant in this experiment because of the near degeneracy of the $I_{5.5}$ and $K_{6.5}$ levels. These fields were not constant in time, but varied slowly over several hours. This made it necessary to establish some convenient method of determining the size of the stray field frequently during the course of a data run. For this purpose, the $H_{4.5}$-$I_{5.5}$ transition near 1400 MHz was chosen, since it was easy to observe quickly with reasonable signal to noise. The position of this resonance, denoted here as "D," was measured several times during each data run. The variation in its position was found to be consistent with a linear drift in stray field, and such a linear fit was used to associate a position of this resonance with each measurement of other frequency intervals, in anticipation of the need for Stark shift corrections.

In order to make such corrections, it was necessary to establish the following: (1) D_0, the position of the field-monitor transition, D, in the absence of stray fields and (2) the ratio of the Stark shift rate of each of the other measured intervals to the Stark shift rate of the transition D.

The first of these was determined in two ways. The simplest method took advantage of the correlation between Stark shift and Stark broadening of this transition. Over the course of this study the transition D was measured 30 times. Its position varied by around 3 MHz and its width by a similar amount. The strong correlation between the observed width and position made it possible to estimate the position that would correspond to the width of an unbroadened line. The result was D_0=1397.91(49) MHz. A second, more complicated method of determining D_0 took advantage of the older measurement of the $K_{6.5}$-$L_{7.5}$ transition, which we refer to as F. In the earlier measurement, with smaller stray fields present, it was possible to use observations of the 27^1D_2-27^1F_3 transition in helium, whose unperturbed frequency has been precisely calculated [4] to infer a value for the ambient stray field. Using observations of this helium transition in close time proximity to the measured $K_{6.5}$-$L_{7.5}$ transition, and making a small Stark shift correction depending on the calculated relative shift rate of the two transitions, it was determined that at zero stray field

F_0=302.25(7) MHz, where the uncertainty is primarily due to assuming a 30% uncertainty in the relative Stark shift rates. An independent estimate of the same interval was obtained by the same procedure of extrapolating observed frequency vs linewidth, described above for the D transition. This gave a consistent result of F_0=301.98(9) MHz. The average of these two independent determinations is F_0=302.12(14) MHz.

Once F_0 is known the several observations of this transition in close time proximity to the D transition could be used to determine D_0. An extrapolation to the F_0 position gave D_0=1398.18(22) MHz. This is consistent with and somewhat more precise than the simpler method. The weighted average of these two independent estimates is

$$D_0 = 1398.13(20)\ \text{MHz}.$$

The second ingredient necessary for calculating Stark shift corrections is the ratio of the Stark shift rate of each transition to that of the D transition. Once the approximate fine-structure level pattern is known, these can be readily calculated for each m_K state using second-order perturbation theory and an average shift rate calculated assuming equal population of the m states. The results of this procedure are shown in column 2 of Table III.

The accuracy of the shift rates are difficult to assess for many of the transitions because the Stark shifts are so small as to be barely noticeable. However, four of the transitions showed easily resolved shifts of up to a MHz or more. These four transitions provide an opportunity to check the accuracy of the calculated relative shift rates, at least for this subset of the transitions. This is accomplished by plotting the measured frequency of each transition vs the frequency difference of the inferred position of the D transition at the time of the measurement from D_0 and fitting this to a linear curve to infer the relative Stark shift rates of the two transitions. The results of this test, shown in Table IV, indicate agreement between measured and calculated Stark shift rate ratios at the level of about 30%.

Stark shift corrections were calculated for all the transitions, using the inferred value of the D transition at the time of the measurement. The correction, Δf_E, was calculated using

$$\Delta f_E = -(D - D_0)R_i,$$

where R_i is the estimated shift rate ratio for the interval, shown in column 3 of Table III, taken to be uncertain by 30%.

The corrected results for the twenty-one frequency intervals measured in this study are summarized in the final column of Table II. Column 4 shows the average Stark shift correction to each interval, along with the uncertainty assigned to the correction. Column 5 shows the additional uncertainty assigned in cases where the two spin components were unresolved. Column 6 shows the statistical uncertainty assigned to the corrected intervals, again taken to be the larger of the internal or external errors of the mean. The reduced statistical uncertainty, compared to column 3 indicates that the Stark shift correction reduces the scatter in the repeated measurements. The final corrected result is shown in column 7 of Table III, with an uncertainty that combines the uncertainties from columns 4, 5, and 6.

TABLE III. Calculated Stark shift rates for transitions in this study. Column 1 identifies the transition and column 2 gives the Stark shift rate calculated under the assumption of equal contributions of all m_K states to the measured resonance. Note the very large shift rates of transitions involving either the $I_{5.5}$ or the $K_{6.5}$ level. Column 3 gives the ratio between the shift rate for each transition and that for the "D" transition, $H_{4.5}$-$I_{5.5}$.

Transition	Shift rate $[\text{MHz}/(\text{V}/\text{cm})^2]$	Rate/D rate
$H_{3.5}$-$I_{4.5}$	−0.11	−0.0006
$H_{3.5}$-$K_{5.5}$	−0.05	−0.0003
$H_{4.5}$-$I_{5.5}$	184.6	1
$H_{5.5}$-$I_{5.5}$	−168.9	−0.91
$H_{5.5}$-$I_{6.5}$	13.08	0.07
$H_{6.5}$-$I_{7.5}$	−0.16	−0.0009
$I_{4.5}$-$K_{5.5}$	0.01	0.0001
$I_{6.5}$-$K_{6.5}$	147.8	0.80
$I_{6.5}$-$K_{7.5}$	−0.16	−0.0009
$I_{7.5}$-$K_{8.5}$	0.04	0.0002
$K_{5.5}$-$L_{6.5}$	0.38	0.0021
$K_{6.5}$-$L_{7.5}$	−144.9	−0.78
$K_{7.5}$-$L_{7.5}$	3.14	0.017
$K_{7.5}$-$L_{8.5}$	0.57	0.0031
$K_{8.5}$-$L_{9.5}$	0.48	0.0026
$L_{6.5}$-$M_{7.5}$	0.86	0.0047
$L_{7.5}$-$M_{7.5}$	−3.75	−0.020
$L_{7.5}$-$M_{8.5}$	0.67	0.0036
$L_{8.5}$-$M_{8.5}$	−3.24	−0.018
$L_{8.5}$-$M_{9.5}$	1.33	0.0072
$L_{9.5}$-$M_{10.5}$	1.24	0.0067
$L_{9.5}$-$M_{9.5}$	−1.62	−0.0088

The 21 measured intervals determine the relative positions of the 20 energy levels with $L \geqslant 5$ in the n=10 Ar fine structure. Since absolute energies cannot be determined from these measurements, the $M_{8.5}$ state was chosen as a reference

TABLE IV. Results of linear fits measuring the correlation between the observed frequency of four transitions and the inferred position of the D transition at the time of the measurement. The second column gives the fitted slope, which is interpreted as the ratio of the transition's Stark shift rate to the Stark shift rate of the D transition. The third column is the calculated ratio, from Table III. The ratio between observed and predicted shift rate ratios is shown in column 4.

Transition	Observed ratio	Predicted ratio	Observed/Predicted
$H_{5.5}$-$I_{5.5}$	−0.63(4)	−0.91	0.69(4)
$H_{5.5}$-$I_{6.5}$	0.066(11)	0.071	0.93(16)
$I_{6.5}$-$K_{6.5}$	0.45(21)	0.80	0.56(26)
$K_{6.5}$-$L_{7.5}$	−0.97(15)	−0.78	1.24(19)

TABLE V. Table of measured energies relative to $(3/2)10M_{8.5}$. The $n=10$ Rydberg levels are identified in column 1. Column 2 gives the measured energies. Columns 3 and 4 show the small contributions to the energies from relativistic and second-order energies that are subtracted from the energies to form a result, $E^{[1]}$, that should be equivalent to the expectation value of $V_{eff.}$, from which the Ar$^+$ core properties can be determined.

State (L_K)	E^{Obs} (MHz)	E^{Rel} (MHz)	$E^{[2]1}$ (MHz)	$E^{[1]}=E^{Obs}-E^{Rel}-E^{[2]}$
$F_{3.5}$	−22253(30)	N/A	N/A	N/A
$H_{3.5}$	−21192.69(6)	−18.71	117.1(1.4)	−21291.1(1.4)
$H_{4.5}$	−766.613(99)	−18.71	−46.57(4)	−701.3(1.0)
$H_{5.5}$	5020.91(7)	−18.71	−85.72(25)	5125.33(26)
$H_{6.5}$	−15690.38(8)	−18.71	−112.38(36)	−15559.29(37)
$I_{4.5}$	−11807.97(6)	−13.81	68.30(14)	−11862.46(15)
$I_{5.5}$	631.49(98)	−13.81	−8.86(0)	654.16(98)
$I_{6.5}$	3566.74(6)	−13.81	−27.57(3)	3608.13(6)
$I_{7.5}$	−8963.70(8)	−13.81	−32.90(3)	−8916.98(9)
$K_{5.5}$	−7497.78(6)	−10.22	33.52(1)	−7521.08(6)
$K_{6.5}$	611.86(12)	−10.22	1.65(0)	620.43(12)
$K_{7.5}$	2256.63(6)	−10.22	−7.92(0)	2274.77(6)
$K_{8.5}$	−5895.94(8)	−10.22	−11.43(0)	−5874.30(8)
$L_{6.5}$	−5298.91(5)	−7.47	−18.05(0)	−5273.40(5)
$L_{7.5}$	309.75(2)	−7.47	1.43(0)	315.79(2)
$L_{8.5}$	1302.90(5)	−7.47	−2.99(0)	1313.36(5)
$L_{9.5}$	−4294.29(8)	−7.47	−4.39(0)	−4282.43(8)
$M_{7.5}$	−4003.90(5)	−5.30	−1.28(0)	−3997.31(5)
$M_{8.5}$	0.00	−5.30	0.83(0)	4.47(0)
$M_{9.5}$	634.70(5)	−5.30	−1.27(0)	641.26(5)
$M_{10.5}$	−3372.85(9)	−5.30	−1.80(0)	−3365.75(9)

state for relative energies, and its energy was taken to be zero. The relative energies of the remaining 19 states are computed by adding and subtracting the appropriate transition intervals. In the two cases where a level position is over determined by the data, the resulting relative energies were determined using a weighted average. The final results are shown in column 2 of Table V.

The energies tabulated in Table V are given with respect to the $10M_{8.5}$ level. This is necessary if the full precision of the microwave measurements is to be retained. For other purposes, it may be useful to know the energies of these same levels with respect to either the ground state of neutral argon or of the Ar$^+$ ion. With respect to the $^2P_{3/2}$ ground state of Ar$^+$, the energy of the $10M_{8.5}$ level can be calculated within the effective potential model as

$$E((^2P_{3/2})10M_{8.5}) = E(^2P_{3/2}) - \frac{\mathrm{Ryd}_{\mathrm{Ar}}}{10^2} + E_{rel}(10M) + E^{[1]}(10M_{8.5}) + E^{[2]}(10M_{8.5}). \qquad (5)$$

The last two terms may be calculated using the Ar$^+$ core parameters determined in this paper, and E_{rel} can be calculated from Eq. (10) below. The results are

$$E_{rel}(10M) = -5.3\ \mathrm{MHz} = -0.000\,18\ \mathrm{cm}^{-1},$$

$$E^{[1]}(10M_{8.5}) = +1204.4\ \mathrm{MHz} = +0.040\,17\ \mathrm{cm}^{-1},$$

$$E^{[2]}(10M_{8.5}) = +0.8\ \mathrm{MHz} = +0.000\,03\ \mathrm{cm}^{-1}.$$

Then,

$$E((^2P_{3/2})10M_{8.5}) = E(^2P_{3/2}) - (1097.358\,11 + 0.000\,18 - 0.040\,17 - 0.000\,03)\ \mathrm{cm}^{-1},$$

$$E(^2P_{3/2}) - 1097.318\,09\ \mathrm{cm}^{-1} = E(^2P_{3/2}) - 32\,896\,768.7\ \mathrm{MHz}. \qquad (6)$$

The energy of the $10M_{8.5}$ level with respect to the ground state of neutral argon can only be given to the precision with which the first ionization threshold of argon is known from other measurements. That value is given as $E_I = 127\,109.80\ \mathrm{cm}^{-1}$ [10], making the energy of the reference $10M_{8.5}$ level relative to the argon ground state $126\,012.49\ \mathrm{cm}^{-1}$.

IV. CORE PROPERTIES

A. The effective potential model

The fine-structure patterns in nonpenetrating high-L Rydberg states can be conveniently expressed in terms of an effective potential that describes the long-range interactions between the Rydberg electron and the positively charged ion core. The form of the potential can be derived from the nonrelativistic Hamiltonian for the full system by assuming that the single Rydberg electron is distinguishable from all the core electrons and always further from the nucleus than any of the core electrons. Thus

$$H = (H_{core} + H^0_{Ryd}) + \sum_{\kappa=1}^{\infty} \sum_{i=1}^{N-1} r_i^{\kappa} C^{\kappa}(\hat{r}_i) \cdot \frac{C^{\kappa}(\hat{r})}{r^{\kappa+1}}, \qquad (7)$$

where r_i and r represent the coordinates of the $N-1$ core electrons and the Rydberg electron, respectively, and $C^{[\kappa]}(\hat{r})$ is a spherical tensor. The zero-order Rydberg wave functions are fully screened hydrogenic functions and are completely known. The eigenfunctions and eigenvalues of H_{core} are of course much more complicated and are not known, but the perturbation energies turn out to depend only on a small number of parameters that can be written in terms of core ion matrix elements and energies. The derivation of the effective potential is carried out using the method developed by Drachman, for helium Rydberg states [11], relying on a formal expansion of the energy denominators occurring in perturbation theory and on the analytic properties of hydrogenic wave functions. The form of the effective potential for $^2S_{1/2}$ core ions has recently been discussed and extended by Snow, using this method [12]. For a $^2P_{3/2}$ core ion, such as Ar$^+$, the derivation is more involved and the result contains scalar, vector, and tensor terms. The form of the effective potential in this case is found to be

$$
\begin{aligned}
V_{eff} = &-\left(\frac{\alpha_{d,0}}{2r^4} + \frac{(\alpha_{Q,0} - 6\beta_{d,0})}{2r^6} + \cdots\right) \\
&-\left(\frac{g_J\alpha^2}{2r^3} - \frac{\beta_{d,1}}{r^6} + \cdots\right)\vec{L}\cdot\vec{J}_c \\
&-\left(\frac{Q}{r^3} + \frac{\alpha_{d,2}}{2r^4} + \frac{(\alpha_{Q,2} + \alpha_{dO,2} - 6\beta_{d,2})}{2r^6} + \cdots\right) \\
&\times \frac{X^{[2]}(J_c)\cdot C^{[2]}(\hat{r})}{\begin{pmatrix} 3/2 & 2 & 3/2 \\ -3/2 & 0 & 3/2 \end{pmatrix}} + \cdots ,
\end{aligned}
\tag{8}
$$

in which $X_c^{[2]}$ is a second rank unit tensor in the space of the core ion. The symbol in the denominator is a 3-j symbol, and α is the fine-structure constant. The coefficients that appear in V_{eff} are properties of the $^2P_{3/2}$ ground state of Ar$^+$: Q, electric quadrupole moment; $\alpha_{\mathrm{d},0}$, scalar dipole polarizability; $\alpha_{\mathrm{d},2}$, tensor dipole polarizability; $\alpha_{\mathrm{Q},0}$, scalar quadrupole polarizability; $\alpha_{\mathrm{Q},2}$, tensor quadrupole polarizability; $\alpha_{\mathrm{dO},2}$, tensor dipole octupole polarizability; $\beta_{\mathrm{d},0}$, scalar nonadiabatic dipole polarizability; $\beta_{\mathrm{d},1}$, vector hyperpolarizability; $\beta_{\mathrm{d},2}$, tensor dipole nonadiabatic polarizability. Each of these is given explicitly in terms of matrix elements and excitation energies of Ar$^+$ in Appendix B.

The term in V_{eff} proportional to Q results from the first-order perturbation energy from the Coulomb perturbation in Eq. (4). The terms proportional to some version of α are adiabatic terms in the second-order dipole and quadrupole perturbation energies. Those proportional to some version of β result from the first nonadiabatic corrections to the second-order dipole perturbation energy. The vector term, proportional to $\beta_{\mathrm{d},1}$, has been previously discussed [13,14]. The other two nonadiabatic terms are similar to terms derived by a different method [14]. Additional contributions proportional to higher inverse powers of r are omitted, in this approximation. The term proportional to g_J is an *ad hoc* addition describing the magnetic interactions between the Rydberg electron's motion and the core ion's magnetic moment, which, of course, is omitted from Eq. (7).

The nonrelativistic energy levels for a nonpenetrating high-L electron are given in terms of V_{eff} by

$$
\begin{aligned}
E((J_c)nL_K) = {}& E^0(J_c,n) + \langle (J_c)nL_K|V_{eff}|(J_c)nL_K\rangle \\
&+ \sum_{n',L',J'_C} \frac{|\langle (J_C)nL_K|V_{eff}|(J'_C)n'L'_K\rangle|^2}{[E_C(J_C) + E^0(n)] - [E_C(J'_C) + E^0(n')]},
\end{aligned}
\tag{9}
$$

where J_C and J'_C refer to the two fine-structure levels of the ^2P ground state of Ar$^+$, and nL_K refers to a specific Rydberg level, ignoring the Rydberg electron's spin. The first term in Eq. (9) describes the zero-order energy of a Rydberg level, which is the same for all of the $n=10$ levels studied here. The second and third terms then will describe the fine-structure pattern, representing the first- and second-order perturbation energies produced by the effective potential. The second term is by far dominant. The third term describes the mixing of different Rydberg series as long as these are produced by long-range interactions between nonpenetrating states. Omitted from Eq. (9) are the small L-dependent relativistic corrections to the energy of hydrogenic levels, which will be treated separately.

B. Extraction of structure factors from measured level positions

The measured relative energies of the twenty $n=10$ argon fine-structure levels summarized in Table V contain a great deal of information about the Ar$^+$ core ion. The most convenient way to extract this information is to isolate the most significant part of the pattern by removing the small contributions from (a) the relativistic corrections to the hydrogenic energy of the Rydberg electron, and (b) the second-order effects of V$_{\mathrm{eff}}$, represented by the last term in Eq. (9), leaving a result that should be equivalent to a simple expectation value of V_{eff}. The first of these comes from the "p^4" term only since the measured level pattern corresponds to the center of gravity of the two spin-orbit levels. It is given by

$$
E^{rel} = \frac{\alpha^2}{2n^4}\left(\frac{3}{4} - \frac{n}{L+\frac{1}{2}}\right).
\tag{10}
$$

The second small contribution, which we denote as $E^{[2]}$, represents the effects of mixing between different Rydberg series as approximated by the last term in Eq. (9). It is, of course, necessary to have values of the core properties occurring in V_{eff} before $E^{[2]}$ for each level can be calculated. Initially, we used the core properties determined in an earlier study [6] to make an evaluation of $E^{[2]}$ for each of the levels studied here. Subsequently, after core properties were determined from that analysis, the calculations of $E^{[2]}$ were repeated with the newly determined values and the procedure iterated until no further change in the derived properties was seen. The calculated values of $E^{[2]}$ were obtained in two ways, by explicit summation over discrete states and numerical integration over continuum states, and by use of the Dalgarno-Lewis method, where the solution of a differential equation replaces the sum and integral [15]. The agreement between the two methods gives confidence in the numerical methods used. The accuracy of these calculated corrections is limited by the accuracy of the coefficients used for each term and by the convergence of the sequence of terms in V_{eff}. The uncertainties shown in Table V are the quadrature sum of 0.1% of the total shift, to account for the parameter precision, and the contribution of the smallest term, to account for the convergence. Both the E^{rel} and the $E^{[2]}$ contributions are shown in Table V for each of the levels studied, along with the inferred first-order perturbation energies, $E^{[1]}$,

$$
E^{[1]} = E^{obs} - E^{rel} - E^{[2]},
\tag{11}
$$

which should represent the expectation value of V_{eff} in the state of interest.

It is expected that $E^{[1]}$ can be decomposed into scalar, vector, and tensor parts,

TABLE VI. Scalar, vector, and tensor components of the energy for each value of L studied here, determined by a weighted fit of Eq. (12). The $H_{3.5}$ data for $L=5$ has been omitted for reasons discussed in the text.

L	A_0 (MHz)	A_1 (MHz)	A_2 (MHz)	RMS deviation (MHz)	χ^2
5	−7598.56(68)	−1.02(14)	20677.91(90)	—	—
6	−3902.72(6)	−0.704(9)	12519.75(9)	0.57	0.37
7	−2515.16(8)	−0.520(10)	8144.69(15)	0.08	2.13
8	−1923.28(7)	−0.376(8)	5592.06(12)	0.063	5.81
9	−1646.03(4)	−0.269(4)	4004.08(6)	0.039	1.68

$$E^{[1]} = A_0(n,L) + A_1(n,L)(\vec{J}_c \cdot \vec{L}) + A_2(n,L)(T^2_{J_c} \cdot T^2_{Ryd}), \tag{12}$$

where A_0, A_1, and A_2 are the scalar, vector, and tensor structure factors for each nL state,

$$\vec{J}_c \cdot \vec{L} \equiv \frac{1}{2}[K(K+1) - J_c(J_c+1) - L(L+1)], \tag{13}$$

and

$$\langle T^2_{J_c} \cdot T^2_{Ryd} \rangle \equiv \frac{\langle X^{[2]}(J_c) \cdot C^{[2]}(\hat{r}) \rangle}{\begin{pmatrix} 3/2 & 2 & 3/2 \\ -3/2 & 0 & 3/2 \end{pmatrix}}$$

$$= \frac{(-1)^{3/2+K}(2L+1)\begin{Bmatrix} K & L & \frac{3}{2} \\ 2 & \frac{3}{2} & L \end{Bmatrix}\begin{pmatrix} L & 2 & L \\ 0 & 0 & 0 \end{pmatrix}}{\begin{pmatrix} \frac{3}{2} & 2 & \frac{3}{2} \\ -\frac{3}{2} & 0 & \frac{3}{2} \end{pmatrix}}. \tag{14}$$

The degree to which the measured level pattern conforms to Eq. (12) is a significant check on the assumptions of this analysis and of our estimates of uncertainty. The fits to Eq. (12) show that the $10I$, K, L, and M levels conform to this pattern approximately within the estimated statistical errors. Table VI shows the rms deviation between the fit and the data for each of these cases, as well as the reduced χ^2 of the fits. In each of these cases, the uncertainties in the fitted parameters A_i were expanded by the square root of the reduced χ^2 to avoid underestimating the parameter errors. The $10H$ levels, however, do not conform to the pattern given by Eq. (12) even approximately. The fit to all four $10H$ levels results in a reduced χ^2 greater than 5000. This is due to the significant perturbation of the $10H_{3.5}$ state by the mixing with the $10F_{3.5}$ state, discussed in Appendix A, a perturbation that is not well described by our model because the $10F_{3.5}$ state is not a high-L state. Consequently, the $10H_{3.5}$ level was excluded from the fit to Eq. (12), and the remaining three levels were fit to determine the structure factors for the H levels. This fit, of course, is exact, since there is no longer any redundancy to the pattern. The results are shown in Table VI. In retrospect, when the expected position of the $H_{3.5}$ state is calculated, using the values of A_0, A_1, and A_2, found from the other three H states, the result is 81(2) MHz lower than its observed energy, indicating the approximate average energy shift due to perturbation by the $F_{3.5}$ level.

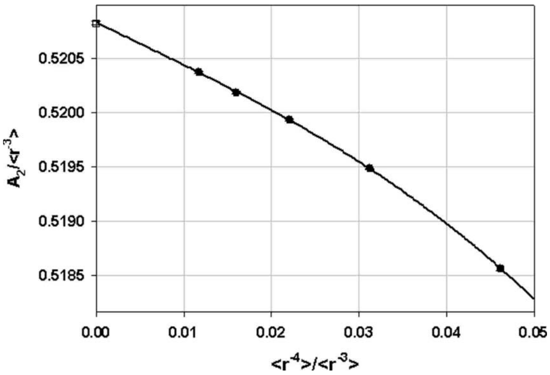

FIG. 7. Plot of the scaled tensor structure factors, A_2, for the $L=5$, 6, 7, 8, and 9 levels. The fitted curve given by Eq. (15) is shown as a solid line. Q and $\alpha_{d,2}$ are determined from the intercept and slope of the fit, respectively. Higher-order contributions leading to an apparent curvature of the data are accounted for by the inclusion of the B_6^T parameter in the fitting function. The point on the y-axis illustrates the fitted intercept. The error bars on the points lie within the points themselves.

C. Determination of core properties

Once the structure factors for each nL level are known, their variation with L can be used to separate the contributions proportional to different powers of r. To illustrate this procedure, consider first the tensor factor, A_2. Since the leading term of this type in V_{eff} is proportional to r^{-3}, it is convenient to scale the measured structure factors by the expectation value of r^{-3} in each nL level. The scaled values are expected to be of the form

$$\frac{A_2(n,L)}{\langle r^{-3}\rangle_{nL}} = B_3^T + B_4^T\frac{\langle r^{-4}\rangle}{\langle r^{-3}\rangle} + B_6^T\frac{\langle r^{-6}\rangle}{\langle r^{-3}\rangle} + \cdots , \tag{15}$$

where the radial expectation values are taken to be hydrogenic values [16] corrected for the finite mass of the Ar$^+$ ion core. The plot of scaled tensor structure factors in Fig. 7, shows an excellent fit to Eq. (14) with

$$B_3^T = 0.520\,83(2), \quad B_4^T = -0.0384(9), \quad B_6^T = -3.2(3).$$

Comparing with the form of V_{eff}, the fitted coefficients B_3^T and B_4^T lead to determinations of the quadrupole moment and the adiabatic tensor dipole polarizability,

$$Q = -B_3^T = -0.520\,83(2) \text{ a.u.},$$

$$\alpha_{d,2} = -2B_4^T = 0.077(2) \text{ a.u.}$$

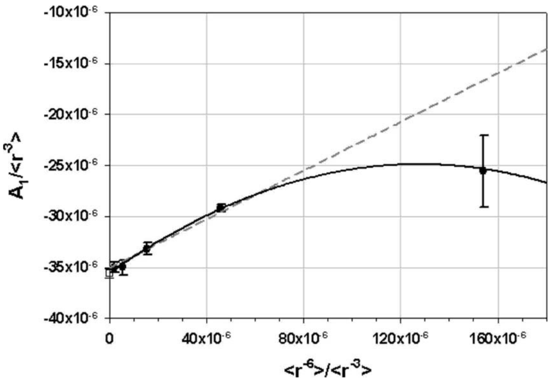

FIG. 8. Plot of the scaled vector structure factors, A_1, for $L=5$, 6, 7, 8, and 9. The dashed line represents the straight line fit, given by Eq. (16) and the solid line represents the improved fit using Eq. (17). The intercept and initial slope of the fit determine the g factor of Ar$^+$ and the vector hyperpolarizability $\beta_{d,1}$, respectively. The point on the y axis illustrates the fitted intercept.

Since the leading contribution to the vector structure factors is also proportional to r^{-3}, most of the variation with L can be removed by again scaling the results by the expectation value of r^{-3}. The resulting plot, shown in Fig. 8, illustrates the variations with L that remain after this scaling. The form of V_{eff} shown in Eq. (5) suggests that these scaled results should lie on a straight line when plotted, as shown, vs the ratio of $\langle r^{-6}\rangle$ to $\langle r^{-3}\rangle$. The dashed line in Fig. 8 is a fit of the data to the form

$$\frac{A_1(n,L)}{\langle r^{-3}\rangle_{nL}} = B_3^V + B_6^V\frac{\langle r^{-6}\rangle}{\langle r^{-3}\rangle} \tag{16}$$

with

$$B_3^V = -3.503(65)\times 10^{-5},$$

$$B_6^V = 0.119(19).$$

The term proportional to B_6^V comes from the first nonadiabatic correction to the dipole polarizability. There could well be subsequent nonadiabatic dipole terms and nonadiabatic terms from higher multipoles that could produce vector terms proportional to higher inverse powers of r. If present, these higher terms could produce curvature in the plot in Fig. 9, as is suggested by the data. In spite of the absence of any theoretical prediction of vector terms proportional to higher inverse powers of r, it is nevertheless instructive to fit the data to the expanded form,

$$\frac{A_1(n,L)}{\langle r^{-3}\rangle_{nL}} = B_3^V + B_6^V\frac{\langle r^{-6}\rangle}{\langle r^{-3}\rangle} + B_8^V\frac{\langle r^{-8}\rangle}{\langle r^{-3}\rangle}. \tag{17}$$

This leads to the solid line shown in Fig. 9 and the coefficients

$$B_3^V = -3.558(44)\times 10^{-5},$$

$$B_6^V = 0.184(26),$$

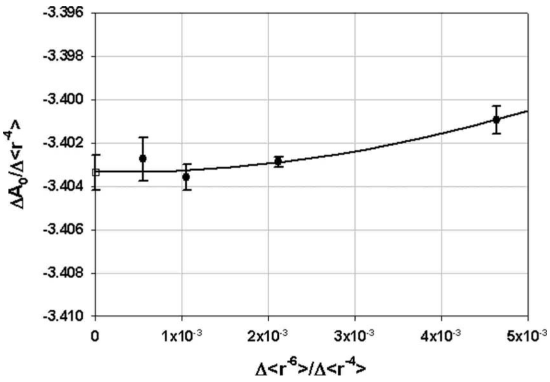

FIG. 9. Plot of the scaled scalar structure factors, A_0, versus L for $n=10$ Rydberg levels of Ar. The solid line represents the fit to the curve given by Eq. (19). The point on the y axis illustrates the fitted intercept, which determines the scalar dipole polarizability of Ar$^+$.

$$B_8^V = -21(8).$$

The second fit is a much better match to the data, with the reduced χ^2 smaller by a factor of 3. It seems to be a more reliable estimate of the initial slope and intercept. The fitted values lead to

$$g_J = \frac{-2}{\alpha_{FS}^2}B_3^V = 1.335(17),$$

$$\beta_{d,1} = B_6^V = 0.184(26)\text{ a.u.}$$

The value of g_J is consistent with 4/3, the value expected for Russell-Saunders (LS) coupling in a $^2P_{3/2}$ state. The value of $\beta_{d,1}$ represents only the second measurement of such a parameter. A similar analysis of $n=10$ fine structure in neon found a value of $\beta_{d,1}$=0.031(19) a.u., considerably smaller than the value found here. We note that in that report, since the origin of the term was not yet clear, it was denoted C_Φ [2].

The contributions to the scalar terms in the fine-structure pattern cannot be treated in quite so direct a manner since only the relative energies, not absolute energies, were determined by experiment. The values of A_0 shown in Table VI therefore contain an arbitrary offset, necessary to set the energy of the $M_{8.5}$ level to zero. The variation of A_0 with L is displayed by the differences between A_0's in adjacent L levels. Since the leading scalar term in V_{eff} is proportional to r^{-4}, most variation with L can be suppressed by normalizing these differences to the difference of the corresponding expectation values of r^{-4}. Defining

$$\Delta A_0(L,L+1) \equiv A_0(L+1) - A_0(L),$$

$$\Delta\langle r^{-s}\rangle_{L,L+1} \equiv \langle r^{-s}\rangle_{L+1} - \langle r^{-s}\rangle_{L}, \tag{18}$$

and scaling the values of ΔA_0 by the corresponding values of $\Delta\langle r^{-4}\rangle$ leads to the plot shown in Fig. 9. Also shown in Fig. 9 is a fit to the function

TABLE VII. Core properties for Ar$^+$ and Ne$^+$. Column 2 shows the Ar$^+$ properties determined from this study, which improves upon the precision of the results in column 3 from the previous optical study of argon [6] by an order of magnitude or more. Columns 4 and 5 show determinations of similar properties of the Ne$^+$ ion, using the experimental data of Ref. [2]. Column 6 shows some theoretical calculations of Ne$^+$ properties for comparison. No similar theoretical values are yet known for Ar$^+$.

	Ar$^+$		Ne$^+$		
Core property	Present work (a.u.)	Wright *et al.*[a] (a.u.)	Ward *et al.*[b] (a.u.)	Clark *et al.*[c] (a.u.)	Theory
Q	−0.52083(2)	−0.517(2)	−0.20403(5)	−0.204020(5)	−0.2032(5)[d]
$\alpha_{d,0}$	6.807(2)	6.83(8)	1.3028(13)	1.3018(2)	1.27[e]
$\alpha_{d,2}$	0.077(2)	−0.07(5)	−0.026(5)	−0.0259(3)	−0.035[f]
g_J	1.335(17)		1.354(21)	1.342(12)	4/3 (LS)
$\beta_{d,1}$	0.184(26)		0.031(19)	0.039(2)	0.0452[e] 0.0479[e]

[a] Wright *et al.* [6].
[b] Ward *et al.* [2].
[c] Clark *et al.* [14].
[d] Sundholm and Olsen [18].
[e] Hibbert *et al.* [19].
[f] Hibbert [20].

$$\frac{\Delta A_0}{\Delta\langle r^{-4}\rangle} = B_4^S + B_6^S\frac{\Delta\langle r^{-6}\rangle}{\Delta\langle r^{-4}\rangle} + B_8^S\frac{\Delta\langle r^{-8}\rangle}{\Delta\langle r^{-4}\rangle}, \qquad (19)$$

which finds

$$B_4^S = -3.4034(9), \quad B_6^S = 0.0(7), \quad B_8^S = 80(92).$$

The fitted value of B_8^S is consistent with zero, but including it in the fit prevents overconfidence in the B_6^S parameter. Similar studies of scalar Rydberg fine-structure pattern have shown that the apparent slope (B_6^S) of such a plot can sometimes be influenced by the contributions of higher-order terms proportional to r^{-7} and $L(L+1)\ r^{-8}$ [12]. In the present case, additional theoretical input will be required to assess whether the simplest interpretation of B_6^S is appropriate. In the meantime, the fitted value of B_4^S allows a determination of the adiabatic dipole polarizability,

$$\alpha_{d,0} = -2B_4^S = 6.807(2)\ \text{a.u.}$$

If complications from higher-order terms are unimportant, which is often the case if the adiabatic expansion is converging well, the coefficient B_6^S contains information about the adiabatic quadrupole polarizability and the first nonadiabatic correction to the dipole polarizability,

$$B_6^S = -\frac{(\alpha_{Q,0} - 6\beta_{d,0})}{2}, \qquad (20)$$

but even in this case, additional theoretical input, such as the distribution of dipole oscillator strengths [17], or a calculation of $\beta_{d,0}$, would be needed to extract the quadrupole polarizability from the data pattern. Even though the parameter B_6^S is consistent with zero, it is likely that a calculation of $\beta_{d,0}$ would yield a nonzero value of α_{Q0}.

V. DISCUSSION

Table VII summarizes the Ar$^+$ properties extracted from this study and from an earlier less precise study of argon Rydberg states [6]. With the exception of $\alpha_{d,2}$, the results are in agreement and much more precise than the earlier measurements. Also shown, for comparison, are the results of a similar study of properties of the Ne$^+$ ground state [2]. In the case of neon, comparison can also be made with the results of an independent analysis of the same experimental data pattern by Clark *et al.*, who used a coupled channels method [14] to extract the same core properties. This resulted in an improved fit of the neon data and correspondingly reduced uncertainties in the extracted parameters. There are many points of similarity between the coupled channels method and the effective potential method used here. Both make the same two fundamental assumptions, neglecting exchange and core penetration, and both invoke essentially identical long-range potentials. The main difference is the method of treating interactions between Rydberg channels and the method of calculating eigenvalues. Both are treated perturbatively in the effective potential method, and nonperturbatively in the coupled channels method. The main advantage of the effective potential method is its simplicity. The assumption of hydrogenic radial functions eliminates the need for any explicit numerical solution of radial equations, which must be done for each separate Rydberg channel in the coupled channels method. Thus the effective potential method is computationally much simpler, but the coupled channels method may ultimately be more precise. Since we have noted in Appendix A that the mixing between the $10H_{3.5}$ and $10F_{3.5}$ levels illustrated in Fig. 10 is difficult to predict with the effective potential method, there is reason to hope that future application of the coupled channels method of analysis to the data reported here may improve the precision of the inferred Ar$^+$ properties, while also including the $H_{3.5}$ level naturally in the analysis.

In the case of neon, comparison can also be made to independent theoretical calculations of the core properties determined from the data. These are shown in column 6 of Table VII. Note the 0.2% agreement with the measured

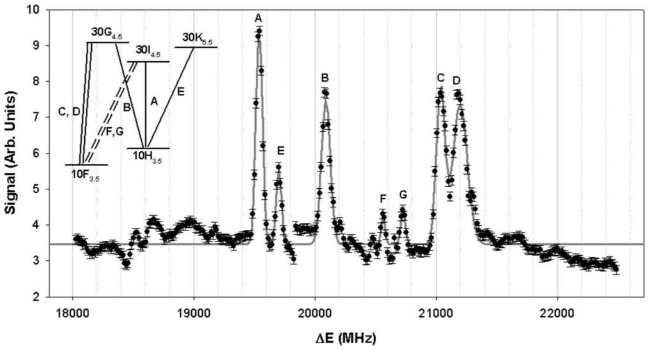

FIG. 10. RESIS optical spectrum determining the position of the $10F_{3.5}$ state relative to the $10H_{3.5}$ state. The x axis is the energy difference of the Doppler tuned laser frequency from the $n=10$ to $n'=30$ hydrogenic energy. The solid line connecting the points represents a seven Gaussian fit that was used to obtain the centers of the signal peaks. The inset level diagram shows the primary states involved in this spectrum. Peak A is the $10H_{3.5}$ to $30I_{4.5}$ transition. Peak B is the $10H_{3.5}$ to $30G_{4.5}$ transition, enhanced by the mixture of $10F_{3.5}$ and $10H_{3.5}$ levels. Peaks C and D are the resolved spin components of the $10F_{3.5}$ to $30G_{4.5}$ transition. Peaks F and G are the spin resolved components of the $10F_{3.5}$ to $30I_{4.5}$ transition, allowed only because of the admixture of $10F_{3.5}$ and $10H_{3.5}$ levels. Peak E is a Stark satellite of Peak A. The existence of peaks F and G is evidence of the mixing between $10F_{3.5}$ and $10H_{3.5}$ levels, and the strength of peaks F and G relative to peaks C and D gives an estimate of the mixing angle. The separation between peak B and peaks C and D gives an estimate of the position of the two spin components of the $10F_{3.5}$ level, relative to the $H_{3.5}$ level.

quadrupole moment and the 2.6% agreement with the measured dipole polarizability. We are unaware of any theoretical predictions of the Ar^+ properties measured here, but a similar comparison will offer a challenging test of the precision of calculated Ar^+ wave functions. The determination of both $\alpha_{d,0}$ and $\alpha_{d,2}$ will pose an especially interesting test, since both are linear combinations of the same set of three dipole matrix element sums, corresponding to $J_C'=\frac{1}{2},\frac{3}{2},\frac{5}{2}$.

The reanalysis of the neon data by Clark *et al.* [14] determined a more precise value of $\beta_{d,1}=0.039(2)$ than obtained with the effective potential analysis, and calculated a theoretical value of 0.0452 or 0.0479 in length and velocity gauges, respectively. In that work, the vector interaction was expressed in slightly different form.

$$V=\beta_V\vec{L}_C\cdot\vec{L},$$

where L_C is the total angular momentum of the core ion, assumed to be in LS coupling. Under those circumstances, the relationship between β_V and $\beta_{d,1}$ is simply

$$\beta_{d,1}=\frac{2}{3}\beta_V.$$

It is interesting to speculate whether the discrepancy between the calculated and fitted values of $\beta_{d,1}$ in Ref. [14] could be related to the possible existence of additional vector terms proportional to higher inverse powers of r, as suggested by Fig. 8. The fitted value of β_6^V from the data in Fig. 8 is quite noticeably altered by the inclusion of the higher-order term in the fit. No such term was included in the analysis of Ref. [14] or that of Ref. [2], nor has it been predicted by any theoretical analysis. Clarifying the expected form of any such higher-order vector terms will be essential to extracting reliable values of $\beta_{d,1}$ from both the neon and argon data.

The main difficulty in this experiment was the presence of Stark shifts due to stray electric fields in the microwave region, which were sometimes as large as 0.2 V/cm. The effects of fields of this size was very noticeable because of the near degeneracy of two of the fine-structure levels central to the fine-structure pattern. Consequently correcting for these Stark shifts became the limiting error in the experiment. Unfortunately, the current design concept for the microwave interaction regions, the eccentric cylindrical TEM transmission line, creates an inherent conflict between the need for wide frequency coverage, which requires small cross sections, and small stray fields, which benefits from larger cross sections. An improved design concept which retains the wide frequency coverage while retaining large cross sections could be an important enhancement of the experimental method.

ACKNOWLEDGMENTS

This work was supported by the Chemical Sciences, Geosciences, and Biosciences Division of the Office of Basic Energy Sciences, Office of Science, U.S. Department of Energy. Laura E. Wright and Phillip L. Jacobson assisted in parts of the experimental work.

APPENDIX A

A possible explanation for the anomalous spin splitting and position of the $H_{3.5}$ level is perturbation by the $F_{3.5}$ level whose unperturbed position could be very close to the $H_{3.5}$ level. Since the $L=3$ $F_{3.5}$ level is not well described as a high-L level, the mixing between this level and the $H_{3.5}$ level and the resulting energy shift of the $H_{3.5}$ level is probably not given accurately by the last term in Eq. (9), $E^{[2]}$. The $(^2P_{3/2})10F_{3.5}$ level has not been previously observed [10], but a rough estimate of its position may be found from the tabulated positions of the analogous $8F_{3.5}$ and $9F_{3.5}$ levels [10]. The quantum defects of these two levels are approximately 0.0035 and 0.0029, respectively. Guessing that the $10F_{3.5}$ state has a quantum defect of 0.0024(10) would put it 16(6) GHz below the $n=10$ hydrogenic level, in close proximity to the $10H_{3.5}$ level at 18.4 GHz below hydrogenic. Another estimate can be obtained from the effective potential model, even though the $10F$ state is far too low in L to really qualify as a high-L level. This predicts that the $10F_{3.5}$ level lies about 0.6 GHz above the $10H_{3.5}$ level. Both estimates, while crude, predict close proximity between these two $K=3.5$ levels, while the other potentially perturbing $10F$ state, with $K=4.5$, is widely separated from the $10H_{4.5}$ level. To investigate this further, the optical spectroscopy in the vicinity of the $10H_{3.5}$-$30I_{4.5}$ level was extended to search for the

$10F_{3.5}$ level and for evidence of mixing between these two levels. Figure 10 shows the result of that search. The line labeled A is the $10H_{3.5}$-$30I_{4.5}$ transition, used to detect microwave transitions involving the $10H_{3.5}$ level. The line labeled E is a Stark-induced satellite transition from $10H_{3.5}$ to $30K_{5.5}$. The splitting between A and E corresponds well to the calculated splitting between the two $n=30$ levels, and the relative strength indicates a stray electric field in the LIR of approximately 0.09 V/cm, consistent with previous studies [6]. None of the other lines, B, C, D, F, and G can be explained except through the presence of the $10F_{3.5}$ level and a substantial mixing between the $H_{3.5}$ and $F_{3.5}$ levels. The inset in Fig. 10, showing the four primary levels involved in these transitions, aids in interpretation of the spectrum. In that inset, the levels are labeled as $H_{3.5}$ and $F_{3.5}$ in spite of the fact that they are significantly mixed,

$$|''F_{3.5}''\rangle = -\sin\theta|H_{3.5}\rangle + \cos\theta|F_{3.5}\rangle,$$

$$|''H_{3.5}''\rangle = \cos\theta|H_{3.5}\rangle + \sin\theta|F_{3.5}\rangle.$$

The line labeled B in Fig. 10 is the transition from the $10H_{3.5}$ level to the $30G_{4.5}$ level, which according to the effective potential model lies about 490 MHz above the $30I_{4.5}$ level. This $\Delta L=-1$ transition is normally quite weak, but it is enhanced by an admixture of the $10F_{3.5}$ state into the $10H_{3.5}$ level. The pair of lines labeled C and D are transitions from the $10F_{3.5}$ level to the same $30G_{4.5}$ level. The separation between the average position of C and D and the line B indicates that the $10H_{3.5}$ level is above the $10F_{3.5}$ level by about 1060(30) MHz, where the uncertainty is due to possible drifts in the CO_2 laser frequency [6]. The splitting between peaks C and D indicates that the two spin components of the $10F_{3.5}$ level are separated by about 160 MHz. Peaks F and G represent transitions between the $10F_{3.5}$ level and the $30I_{4.5}$ level, allowed only by the admixture of the $10H_{3.5}$ state into the $10F_{3.5}$ state. The relative strength of peaks G and D (or F and C) allows an estimate of the mixing angle, Θ, between the $H_{3.5}$ and $F_{3.5}$ levels. The result is approximately 28°. So, the optical spectrum of Fig. 10 confirms both that the $10F_{3.5}$ state is indeed nearly degenerate with the $10H_{3.5}$ state and that the two states are significantly mixed.

The mixing between these two levels offers a plausible explanation for the anomalous spin splitting observed in the $10H_{3.5}$ level. Any scalar operator, O, that does not depend on the spin of the Rydberg electron will have equal matrix elements between the two pairs of unperturbed levels differing in the orientation of Rydberg spin,

$$\langle 10H_{3.5},S_R;J,M|O|10F_{3.5},S_R;J,M\rangle \text{ is independent of } J,M.$$

However, if the unperturbed positions of the $10F_{3.5}$ $J=4$ and 3 levels are significantly different, the energy shift of the $10H_{3.5}$ $J=4$ and 3 levels will be different also, changing the spin splitting in the $H_{3.5}$ level. The order of magnitude of this relative perturbation can be estimated in a simple two-level model. The observed positions of the two $10F_{3.5}$ levels with respect to the (unresolved) position of the two $10H_{3.5}$ levels are approximately 980 and 1140 MHz. Using the approximate mixing angle of 28° and the two-level model, the unperturbed separations for the two pairs of equal J levels are estimated to be 548 and 637 MHz and the energy shifts resulting from the mixing are 216 and 251 MHz, respectively. The 35 MHz relative shift estimated in this way is similar to the observed 15.40(2) MHz increase in the spin splitting compared to the magnetic model. The overestimate may be due to an overestimate of the mixing angle, which seems plausible since the estimate of 28° neglects possible saturation of the lines C and D. A 15 MHz relative shift is consistent with a mixing angle of around 20°, which is also consistent with the smaller average shift of around 80 MHz suggested by the fine-structure analysis. The fact that the $10H_{3.5}$ spin splitting is increased, not decreased, by the mixing indicates that the order of spin levels in the $10F_{3.5}$ state is normal with the $J=4$ level lying above the $J=3$ level by about 160 MHz.

Unfortunately, the coupling necessary to produce the mixing evidenced by Fig. 10 is not simple to include in the effective potential model. The primary tensor coupling in the effective potential is through the quadrupole term in V_{eff}, and for hydrogenic Rydberg radial functions the $\Delta n=0$, $\Delta L=2$ matrix elements of r^{-3} are identically zero. The nonzero coupling due to the tensor polarizability is far too small to account for the degree of mixing seen. The source of the coupling is a second-order coupling via the quadrupole term in the Coulomb perturbation V from Eq. (7),

$$\sum_{n'L'J_c} \frac{\left\langle \left(\frac{3}{2}\right)10F_{3.5}\middle|\overleftrightarrow{Q}\cdot\frac{C^{[2]}}{r^3}\middle|(J_c)n'L'_{3.5}\right\rangle\left\langle (J_c)n'L'_{3.5}\middle|\overleftrightarrow{Q}\cdot\frac{C^{[2]}}{r^3}\middle|\left(\frac{3}{2}\right)10H_{3.5}\right\rangle}{E(10)-[E(J_c)+E(n')]}. \tag{A1}$$

Evaluation of this coupling, using the value of Q determined from the fine-structure pattern gives a coupling of 170 MHz, consistent with the coupling required to cause the degree of mixing evident in Fig. 10. Formally, the energy shift due to this coupling is part of the fourth-order perturbation energy in V. It is unusually significant because of the close proximity of the two equal parity levels $F_{3.5}$ and $H_{3.5}$. The absence of other such near degeneracies in the fine-structure pattern, and the rapid decrease in the magnitude of this second-order coupling with increasing L insures that none of the other fine-structure levels studied here are significantly affected by similar couplings.

APPENDIX B

$$V_{eff} = -\left(\frac{\alpha_{d,0}}{2r^4} + \frac{(\alpha_{Q,0} - 6\beta_{d,0})}{2r^6} + \cdots\right) - \left(\frac{g\alpha_{FS}^2}{2r^3} - \frac{\beta_{d,1}}{r^6} + \cdots\right)\vec{L}\cdot\vec{J}_c - \left(\frac{Q}{r^3} + \frac{\alpha_{d,2}}{2r^4} + \frac{(\alpha_{Q,2} - 6\beta_{d,2})}{2r^6} + \cdots\right) \times \frac{X^{[2]}(J_c)\cdot C^{[2]}(\hat{r})}{\begin{pmatrix} 3/2 & 2\ 3/2 \\ -3/2 & 0\ 3/2 \end{pmatrix}} + \cdots ;$$

explicit forms of the various coefficients occurring in V_{eff} are given below in terms of the reduced matrix elements of the dipole and quadrupole and octupole moment operators, acting on the wave function of the 17 electron Ar$^+$ ion. With the exception of the coefficients $\beta_{d,0}$ and $\beta_{d,2}$, all of these coefficients agree exactly with the coefficients implied by Eqs. (20) and (21) of Ref. [14]. In the two cases where differences occur, agreement would be found if the last terms in Eqs. (28) and (29) of Ref. [14] were neglected,

$$\vec{D} \equiv \sum_{i=1}^{17} r_i C^{[1]}(\hat{r}_i), \quad \overleftrightarrow{Q} \equiv \sum_{i=1}^{17} r_i^2 C^{[2]}(\hat{r}_i), \quad \overleftrightarrow{O} \equiv \sum_{i=1}^{17} r_i^3 C^{[3]}(\hat{r}_i)$$

are

$$Q \equiv -\langle g^2P_{3/2}, m_j = 3/2 | \overleftrightarrow{Q}_0 | g^2P_{3/2}, m_j = 3/2\rangle,$$

$$\alpha_{d,0} \equiv \frac{1}{6}\sum_{\gamma J_c'} \frac{\langle g^2P_{3/2}\|\vec{D}\|\gamma J_c'\rangle^2}{\Delta E(\gamma J_c')},$$

$$\alpha_{d,2} \equiv -\sqrt{\frac{2}{3}}\sum_{\gamma J_c'} \frac{\langle g^2P_{3/2}\|\vec{D}\|\gamma J_c'\rangle^2}{\Delta E(\gamma J_c')}(-1)^{3/2-J_c'}\begin{Bmatrix} J_c' & 3/2 & 1 \\ 2 & 1 & 3/2 \end{Bmatrix},$$

$$\alpha_{Q,0} \equiv \frac{1}{10}\sum_{\gamma J_c'} \frac{\langle g^2P_{3/2}\|\overleftrightarrow{Q}\|\gamma J_c'\rangle^2}{\Delta E(\gamma J_c')},$$

$$\alpha_{Q,2} \equiv \sqrt{\frac{2}{7}}\sum_{\gamma J_c'} \frac{\langle g^2P_{3/2}\|\overleftrightarrow{Q}\|\gamma J_c'\rangle^2}{\Delta E(\gamma J_c')}(-1)^{3/2-J_c'}\begin{Bmatrix} J_c' & 3/2 & 2 \\ 2 & 2 & 3/2 \end{Bmatrix},$$

$$\alpha_{dO,2} \equiv 2\sqrt{\frac{3}{7}}\sum \frac{\langle g^2P_{3/2}\|\overleftrightarrow{Q}\|\gamma J_c'\rangle\langle \gamma J_c'\|\vec{D}\|g^2P_{3/2}\rangle}{\Delta E(\gamma J_c')} \times \begin{Bmatrix} J_c' & 3/2 & 3 \\ 2 & 1 & 3/2 \end{Bmatrix},$$

$$\beta_{d,0} \equiv \frac{1}{12}\sum_{\gamma J_c'} \frac{\langle g^2P_{3/2}\|\vec{D}\|\gamma J_c'\rangle^2}{(\Delta E(\gamma J_c'))^2},$$

$$\beta_{d,1} \equiv \frac{-1}{\sqrt{10}}\sum_{\gamma J_c'} \frac{\langle g^2P_{3/2}\|\vec{D}\|\gamma J_c'\rangle^2}{(\Delta E(\gamma J_c'))^2}(-1)^{3/2-J_c'}\begin{Bmatrix} J_c' & 3/2 & 1 \\ 1 & 1 & 3/2 \end{Bmatrix},$$

$$\beta_{d,2} \equiv \frac{-1}{2\sqrt{6}}\sum_{\gamma J_c'} \frac{\langle g^2P_{3/2}\|\vec{D}\|\gamma J_c'\rangle^2}{(\Delta E(\gamma J_c'))^2}(-1)^{3/2-J_c'}\begin{Bmatrix} J_c' & 3/2 & 1 \\ 2 & 1 & 3/2 \end{Bmatrix}.$$

---

[1] S. R. Lundeen, in *Advances in Atomic, Molecular, and Optical Physics*, edited by Chun C. Lin and Paul Berman (Academic Press, New York, 2005), Vol. 52, pp. 161–208.

[2] R. F. Ward, Jr., W. G. Sturrus, and S. R. Lundeen, Phys. Rev. A **53**, 113 (1996).

[3] E. L. Snow and S. R. Lundeen, Phys. Rev. A **77**, 052501 (2008).

[4] P. L. Jacobson, R. A. Komara, W. G. Sturrus, and S. R. Lundeen, Phys. Rev. A **62**, 012509 (2000).

[5] S. R. Lundeen and C. W. Fehrenbach, Phys. Rev. A **75**, 032523 (2007).

[6] L. E. Wright, E. L. Snow, S. R. Lundeen, and W. G. Sturrus, Phys. Rev. A **75**, 022503 (2007).

[7] C. W. Fehrenbach, S. R. Lundeen, and O. L Weaver, Phys. Rev. A **51**, R910 (1995).

[8] W. G. Sturrus, R. A. Komara, S. R. Lundeen, and P. L. Jacobson, Bull. Am. Phys. Soc. **47**, 65 (2002).

[9] M. A. R. Gunston, *Microwave Transmission Line Impedance Data* (SciTech Publishing, Raleigh, NC, 1997).

[10] Yu. Ralchenko, A. E. Kramida, J. Reader, and NIST ASD Team, NIST Atomic Spectra Database (Version 3.15) (National Institute of Standards and Technology, Gaithersburg, MD, 2008).

[11] R. Drachman, Phys. Rev. A **26**, 1228 (1982), and subsequent papers.

[12] E. L. Snow and S. R. Lundeen, Phys. Rev. A **75**, 062512 (2007).

[13] B. Zygelman, Phys. Rev. Lett. **64**, 256 (1990).

[14] W. Clark, C. H. Greene, and G. Miecznik, Phys. Rev. A **53**, 2248 (1996).

[15] R. A. Komara, W. G. Sturrus, D. H. Pollack, and W. R. Cochran, Phys. Rev. A **59**, 251 (1999).

[16] Kjell Bockasten, Phys. Rev. A **9**, 1087 (1974).

[17] L. J. Curtis, J. Phys. B **40**, 3173 (2007).

[18] D. Sundholm and J. Olsen, Phys. Rev. A **49**, 3453 (1994).

[19] A. Hibbert, M. Le Dourneuf, and Vo Ky Lan, J. Phys. B **10**, 1015 (1977).

[20] A. Hibbert (private communication).